Simplified partitioning model to simulate high pressure under-expanded jet flows impinging vertical obstacles

Jinghu Hu[a], David M Christopher[a,*], Xuefang Li[b,*]

[a]*Key Laboratory for Thermal Science and Power Engineering of Ministry of Education, Department of Energy and Power Engineering, Tsinghua University, Beijing China 100084*
[b]*Institute of Thermal Science and Technology, Shandong University, Jinan China 250061*

Abstract

Various reduced-order models have been developed to quickly model high pressure under-expanded jets. One example is the two-layer partitioning model which was developed to model underexpanded jets, but it has not been evaluated for high pressure jets with obstacles in the jet flow region. This research describes an improved two-layer partitioning model based on the Abel-Noble equation of state that is applied here to model horizontal jet flows impacting a vertical obstacle with validations against high pressure gas experiments, full CFD simulations and a revised notional nozzle model based on the Abel-Noble equation of state. The improved two-layer partitioning model accurately predicts the gas concentrations on the obstacle for a 15 MPa underexpanded jet while consuming much less computational resources and time compared with the full CFD simulation.

Keywords: underexpanded jet, two-layer partitioning model, Abel-Noble gas, hydrogen safety

1. Introduction

Hydrogen, with its low density and low volumetric energy density has to be stored at extremely high pressures for commercial use. A typical commercial hydrogen-fueled vehicle stores hydrogen at 70 MPa with the pressures in fueling station tanks typically reaching 35 MPa. Thus, risk assessments of the high pressure hydrogen storage tanks are necessary for safety evaluations. Protective walls are built around hydrogen storage tanks to prevent high pressure jets from leaks from extending far out into the surrounding area and extending the lower flammability region volume. Thus, detailed descriptions of the flow field for a high pressure, underexpanded jet impacting a vertical obstacle are needed to evaluate and design engineered safety solutions.

*Corresponding author
Email addresses: hujh16@mails.tsinghua.edu.cn (Jinghu Hu), dmc@tsinghua.edu.cn (David M Christopher), lixf@sdu.edu.cn (Xuefang Li)

High pressure underexpanded jet flows will lead to complex nearfield shock structures. Different pressure ratios between the stagnation pressure and the atmospheric pressure lead to different underexpanded nearfield shock structures with four kinds of underexpanded jet flows categorized based on their pressure ratio and, hence, their underexpansion level. Relatively low pressure, underexpanded jets will form a weak shock will the nozzle exit[1, 2]. As the pressure increases, the jet flow becomes moderately underexpanded with diamond shaped oblique shocks[1–5]. The oblique shocks, also called the slip region or the barrel shock region, are reflected to form the reflected oblique shock structure. The reflected oblique shock will regenerate new intersecting shocks when they reach the outer boundary of the jet core region. This cell structure in the slip region tends to repeat itself along the axial direction downstream until the jet reaches ambient pressure. Highly-underexpanded jet flows are characterized by the appearance of a Mach disk at the end of the supersonic jet core region inside the oblique shock structure slip region[6–8]. The Mach disk and the reflected shock intersect at a triple point and the Mach disk is not a perfect flat normal shock but has some curvature. The flow in the slip region continues at a much higher velocity than the flow in the core region after the Mach disk. The slip region can continue to be supersonic with more reflected shocks after the Mach disk location as the slip region expands into the slower core region until become one flow region. In very high pressure underexpanded jets, the slip region normally has a larger area than the potential core region[9, 10]. Air is entrained into the slip region starting shortly after the flow leaves the nozzle with no air entrained into the core flow region. The total jet diameter decreases in very high pressure, underexpanded jets as ambient air is entrained into the flow[11].

Traditional CFD numerical simulations try to solve the Navier-Stokes equations plus other conservation equations throughout the whole simulation geometry, which is called the full CFD simulation model method in this paper. Full CFD simulations are intrinsically unstable when used to simulate supersonic flow shock structures. They require very long computational times and large computational resources for complete high pressure gas flow simulations[12]. Therefore, full CFD simulations are not practical for simulating the large flow fields of underexpanded jets.

In hydrogen safety risk analyses, however, the main interest is the gas concentration profiles in the far field of the underexpanded jet. The underexpanded jet flow profile can then be treated as a relatively simple subsonic compressible flow starting with an already expanded jet based on assumptions about the conservation of mass, momentum and energy[11]. That has given rise to the development of various reduced-order notional nozzle models. The key idea of the notional nozzle models is to predict simplified inlet boundary conditions for underexpanded jet flow simulations. Typical notional nozzle models replace the original high pressure boundary gas inlet condition with fully expanded low pressure velocity/mass inlet(s) boundary conditions which eliminates the nearfield shock structure region and avoids the complex numerical simulations of the shocks. The application of the notional nozzle models still require CFD simulations throughout the extended flow field model geometry. However, the simulations are much more efficient without the need to simulate the shock structures of the high pressure gas inlets. The objective of the simplified notional nozzles is then to predict reasonable gas flow profiles in the jet flow farfield with much faster calculations.

There have been many studies aimed at developing notional nozzle models that give more accurate predictions with more universally applicable simulation conditions. Thring[13] developed the first notional nozzle concept by assuming that the notional nozzle had the same momentum flux and velocity as the real gas nozzle with a gas density equal to that of the gas at ambient conditions. Their model and all other models also assumed an isentropic expansion between the stagnation conditions in the tank to the nozzle. Birch et al.[14] developed a notional nozzle model (Birch84 model) assuming mass conservation between the real nozzle and the notional nozzle without air entrainment. The notional nozzle pressure and temperature were assumed to be the ambient conditions and the gas velocity was assumed to be the local sonic velocity. Many other studies have been inspired by the Birch84 model. The basic assumptions of the Birch84 model, atmospheric pressure in the notional nozzle and the jet flow mass conservation with zero air entrainment, were used as the basic assumptions by many of the following models. Ewan et al.[10] slightly modified the Birch84 model by assuming that the notional nozzle temperature was equal to the real nozzle gas temperature with the other assumptions. Gore et al.[15] developed a modified notional nozzle model based on the momentum conservation assumption between the real nozzle and the notional nozzle. The notional nozzle diameter was assumed to be the same as the real nozzle but with the notional nozzle ambient pressure assumption. Birch et al.[16] gave an improved notional nozzle model (Birch87 model) by adding the momentum conservation assumption in addition to the original mass conservation assumption. The notional nozzle temperature was assumed to be equal to the stagnation temperature of the ideal gas. Several studies have shown that the Birch87 model gives more accurate predictions[16–18]. Yüceil et al.[19] used the atmospheric pressure assumption and the mass, momentum and energy conservation equations to derive a notional nozzle model. Harstad et al.[20] used real underexpanded jet shock structure observations and assumed that the notional nozzle was right after the Mach disk and shared the same diameter as the Mach disk. The flow between the real nozzle and the notional nozzle was assumed to be isentropic with the normal shock wave property relations between the flow before and after the Mach disk used to calculate the notional nozzle profiles. These notional nozzle models were all derived using the ideal gas equation of state (EOS), with later models using a real EOS like the Abel-Noble EOS[21–23].

These notional nozzle models give a simplified method to derive boundary conditions for the notional nozzle that are used as inputs to significantly simplified underexpanded jet flow numerical simulations. However, all these previous notional nozzle models assumed that the gas had uniform velocity and composition distributions at the notional nozzle which is not true in high pressure underexpanded jet flows. Observations have shown that real underexpanded jet flows have complex shock structures, Mach disks and flow stratification between the slip region and the core region with only some of the flow through the Mach disk and most of the high pressure jet flow flowing through the surrounding slip region with air entrainment[24, 25].

Li et al.[17] developed a two-layer partitioning model that takes into account the gas partitioning between the core region and the slip region in real underexpanded jets. The two-layer partitioning model assumed that the gas flows into two separate regions upon exiting the orifice with part of the flow accelerating to very high Mach numbers before passing through the Mach disk where the flow becomes subsonic and part of the flow expanding into the surrounding slip region with air entrainment into this slip region. The gas was modeled using the Abel-Noble EOS inside the storage tank and the ideal gas EOS after leaving the real high pressure nozzle. Such models have been validated for high pressure free jets with stagnation pressures up to 35 MPa. However, given the high stagnation pressure in the tank, the pressure is still much higher than the ambient pressure when choked at the nozzle, so the gas inside the Mach region and possibly inside the slip region should not be treated as an ideal gas. The original two-layer model also did not take into consideration the enthalpy equation for the Abel-Noble EOS. In addition, the validity of two-layer model for predicting high pressure jet flows from an orifice that involves any flow geometry other than a free jet has not been tested.

This research presents an improved version of the two-layer partitioning model to more accurately model high pressure underexpanded jets. The model is applied to the flow of a horizontal jet impacting a vertical obstacle in the flow field. The simulation results are compared with both experimental data and simulation results from other models to validate the partitioning model. The improved two-layer partitioning model can then be used in high pressure hydrogen simulations to evaluate storage safety.

2. Model setup

Two simplified models were used for the simplified numerical simulations with an improved version of the two-layer partitioning model and a revised version of the traditional Birch87 notional nozzle model[16]. The Birch87 model was revised by using the Abel-Noble gas EOS instead of the ideal gas EOS for the density. In both models, the stagnation gas temperature was assumed to be equivalent to the ambient temperature.

2.1. Improved two-layer partitioning model

The notation for the improved two-layer model is shown in Figure 1[17]. The improved two-layer model assumes that the pressure ratio is much larger than the critical pressure for choked flow so the jet flow is extremely underexpanded. In that scenario, the first shock cell is the dominant shock cell in the nearfield shock structure. Some studies have shown that the Mach disk should not be assumed to be a normal shock but the curvature should be taken into account[11]. However, the current study still treats the Mach disk as a normal shock for simplicity.

In the improved two-layer model, the gas was assumed to flow isentropically from stagnation in the tank (state 0) to the real nozzle (state 1). The stagnation pressure was assumed to be higher than the critical pressure so the gas was choked at the real nozzle. After the real nozzle, part of the gas flowed through the core region and reached the Mach disk (state 2a) with the highest velocity occurring just before the Mach disk. After flowing across the shock wave at the Mach disk, the gas pressure returned to the ambient pressure after the Mach disk (state 2b). The rest of the gas expanded out into the slip region, also referred to as the barrel shock region, surrounding the core region with a significant amount of air entrained into the this slip or mixing region. This gas mixture then expanded to atmospheric pressure

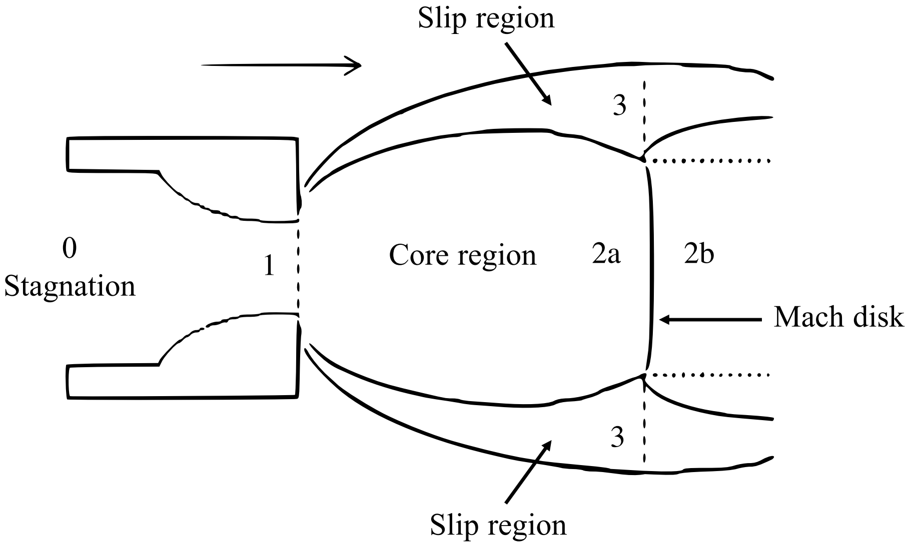

Figure 1: Improved two-layer model notation

(state 3). States 2b and 3 formed the two concentric circle notional nozzle regions of the two-layer partitioning model. In both sections the pressure was assumed to be atmospheric. The flowing gas was modeled using the Abel-Noble EOS throughout the model, while the air entrained into the slip region was assumed to be stagnant before being entrained and was modeled as an ideal gas.

2.1.1. Mass flow rate at the real nozzle

The high pressure gas was assumed to flow from state 0 in the tank and was choked at the orifice at state 1 with the properties at both states satisfying the Abel-Noble EOS[26]:

$$p_1(v_1 - b) = R_g T_1 \tag{1}$$

where v is the specific volume of the gas which is related to the density as $v = \frac{1}{\rho}$, where ρ is the gas density and b is the co-volume coefficient of the gas, which is a constant for each Abel-Noble gas.

The gas velocity at state 1 is equal to the local sound speed so the Mach number is equal to 1. The velocity at state 1 is then given by the sound speed for an Abel-Noble gas[26]:

$$U_1 = \frac{v_1}{v_1 - b}\sqrt{\gamma R_g T_1} \tag{2}$$

The gas flow from the tank to the nozzle is assumed to be an isentropic expansion which for an Abel-Noble is given by[26]:

$$p_0(v_0 - b)^\gamma = p_1(v_1 - b)^\gamma \tag{3}$$

Unlike for an ideal gas, the enthalpy is not just a function of the gas temperature as in an Abel-Noble gas. The equation exists[26]:

$$\frac{\partial h}{\partial p} = b$$

where h is the gas enthalpy. The enthalpy equation of the Abel-Noble gas, therefore, is:

$$h = c_p T + bp$$

The energy equation for an Abel-Noble gas from state 0 to state 1 is then:

$$c_p T_0 + bp_0 = c_p T_1 + bp_1 + \frac{U_1^2}{2} \tag{4}$$

These 4 equations were solved to get the 4 unknowns at the choked nozzle, p_1, T_1, v_1 and U_1. The mass flow rate for the given stagnation pressure and nozzle diameter is then given by:

$$\dot{m}_1 = \frac{U_1 \pi d_1^2}{4 v_1} \tag{5}$$

2.1.2. Mach disk boundary conditions

After the choked orifice, the high pressure flow was assumed to split into the center Mach region and the surrounding slip region. Air was assumed to be entrained into the slip region but not the core with no viscous effects between the slip region and the surrounding air.

The expansion from state 1 to state 2a was also assumed to be isentropic with conservation of the total enthalpy per unit mass from state 1 to state 2a.

$$h_1 = h_2 = c_p T_{2a} + bp_{2a} + \frac{U_{2a}^2}{2} \tag{6}$$

$$p_1 (v_1 - b)^\gamma = p_{2a} (v_{2a} - b)^\gamma \tag{7}$$

The gas was then assumed to cross the Mach disk before reaching state 2b. The post-Mach disk pressure was assumed to be atmospheric. The gas mass, momentum and energy are conserved across the Mach disk.

$$\frac{U_{2a}}{v_{2a}} = \frac{U_{2b}}{v_{2b}} \tag{8}$$

$$p_{2a} + \frac{U_{2a}^2}{v_{2a}} = p_{2b} + \frac{U_{2b}^2}{v_{2b}} \tag{9}$$

$$c_p T_{2a} + bp_{2a} + \frac{U_{2a}^2}{2} = c_p T_{2b} + bp_{2b} + \frac{U_{2b}^2}{2} \tag{10}$$

U_{2a} was supersonic and U_{2b} was subsonic.

The gas was treated as an Abel-Noble gas at states 2a and 2b.

$$p_{2a}(v_{2a} - b) = R_g T_{2a} \tag{11}$$

$$p_{2b}(v_{2b} - b) = R_g T_{2b} \tag{12}$$

The gas properties at states 2a and 2b were found by solving Eqs. 6 to 12. The mass flow rate through the Mask disk was then calculated using:

$$\dot{m}_2 = \frac{U_{2b} \pi d_m^2}{4 v_{2b}} \tag{13}$$

The Mach disk diameter, d_m, was calculated using the equation given by Velikorodny et al.[27]:

$$\frac{d_m}{d_1} = \alpha \frac{z_m}{d_1} \sqrt{1 - \frac{\gamma + 1}{\gamma} \times (\frac{\gamma + 1}{\gamma - 1})^{-0.5}} \tag{14}$$

where α is an empirical constant whose value was set to 0.954 in this research as recommended by the measurements of the hydrogen Mach disk diameter by Li[28]. z_m is the location of the Mach disk which was given by the empirical equation from Li et al.[17]:

$$\frac{z_m}{d_e} = 0.67 \sqrt{\frac{p_0}{p_\infty}} \tag{15}$$

where p_∞ is the ambient pressure.

$\dot{m}_2$, T_{2b}, z_m and d_{2a} were then used as the Mach disk boundary conditions for the improved two-layer partitioning model boundary conditions.

2.1.3. Slip region boundary conditions

In the slip region, the high pressure gas was assumed to entrain air that was originally at zero velocity, atmospheric temperature and atmospheric pressure with the properties satisfying the ideal gas equation. The gas and the air at state 3 were assumed to be uniformly mixed with the gas and the air having the same velocity at atmospheric pressure.

The slip region thickness was calculated using the empirical equation[29]:

$$\frac{B_m}{z_m} = 0.135[1 + \frac{1}{(\frac{p_0}{p_\infty})^{\frac{\gamma-1}{\gamma}}(1 + \frac{\gamma-1}{2})}] \tag{16}$$

When the gas to be simulated was hydrogen instead of helium, the slip region thickness was derived from the empirical equation by Li et al.[17]:

$$\frac{B_m}{d_1} = 0.30 \sqrt{\frac{p_0}{p_\infty}} \tag{17}$$

The slip region area was then:

$$A_{Bm} = (\frac{d_m}{2} + B_m)^2 \pi - \frac{d_m^2 \pi}{4} \tag{18}$$

The mass, momentum and energy equations were then used to determine the conditions of the gas mixture in the slip region:

$$\dot{m}_1 - \dot{m}_2 = \frac{U_3 A_{Bm}}{v_{3,gas}} \tag{19}$$

$$(p_1 - p_\infty)\frac{\pi d_1^2}{4} + \dot{m}_1 U_1 = \dot{m}_2 U_{2b} + U_3^2 A_{Bm}(\frac{1}{v_{3,gas}} + \frac{1}{v_{3,air}}) \tag{20}$$

$$(\dot{m}_1 - \dot{m}_2)(c_p T_1 + b p_1 + \frac{U_1^2}{2}) = U_3 A_{Bm}\frac{c_p T_3 + b p_{3,gas} + \frac{U_3^2}{2}}{v_{3,gas}} + \frac{c_{p3,air}(T_3 - T_\infty) + \frac{U_3^2}{2}}{v_{3,air}} \tag{21}$$

The high pressure gas properties were based on the Abel-Noble EOS, while the entrained air properties were based on the ideal gas EOS:

$$p_{3,gas}(v_{3,gas} - b) = R_g T_3 \tag{22}$$

$$p_{3,air} v_{3,air} = R_{g,air} T_3 \tag{23}$$

where $v_{3,gas}$ and $v_{3,air}$ are the specific volumes of the gas and air and $p_{3,gas}$ and $p_{3,air}$ are the partial pressures of the gas.

The mixture of helium and air satisfies:

$$p_{3,gas} + p_{3,air} = p_3 \tag{24}$$

The slip region gas conditions were then calculated by solving Eqs. 19 to 24. The mass flow rate in the slip region, m_3, and the gas mass fraction, Y, were then calculated using:

$$\dot{m}_3 = U_3 A_{Bm}(\frac{1}{v_{3,gas}} + \frac{1}{v_{3,air}}) \tag{25}$$

and:

$$Y = \frac{U_3 A_{Bm}}{\dot{m}_3 v_{3,gas}} \tag{26}$$

$\dot{m}_3$, T_3, B_m, z_m and Y were then used as the inlet conditions for the slip region inlet boundary conditions of the improved two-layer partitioning model.

The stagnation pressure and temperature in the tank, the nozzle diameter and the ambient pressure were then used to calculate all the parameters for both the Mach disk region and the slip region for the simulations.

2.2. Revised Birch87 model

The traditional notional nozzle model developed by Birch et al.[16] was extended to simulate the high pressure underexpanded jet flow. In the original Birch87 model, the gas was assumed to be an ideal gas. In the current work, the Abel-Noble real gas EOS was used to take into account the real gas effects due to high pressure.

In the revised Birch87 model, the gas was assumed to flow isentropically from the stagnation tank (state 0) to the real nozzle where the flow was choked (state 1). The gas flow was then assumed to have a uniform velocity at the notional nozzle downstream of the real nozzle. The mass and momentum were both conserved between the real nozzle and the notional nozzle. The temperature and pressure of the notional nozzle were assumed to be the known ambient conditions. With the Abel-Noble EOS, the conditions at the notional nozzle (state n) satisfy:

$$p_n(v_n - b) = R_g T_n \tag{27}$$

where $p_n = p_\infty$ and $T_n = T_\infty$.

The mass conservation equations are:

$$\dot{m}_1 = \dot{m}_n = \frac{U_n \pi d_n^2}{4 v_n} \tag{28}$$

while the momentum conservation equation is:

$$(p_1 - p_\infty)\frac{\pi d_1^2}{4} + \dot{m}_1 U_1 = \dot{m}_n U_n \tag{29}$$

The notional nozzle diameter, d_n, and the velocity, U_n, were then determined from Eqs. 27 to 29, with these conditions used for the notional nozzle conditions in the Abel-Noble Birch87 model. The Birch87 model neglects the axial distance between the real nozzle and the notional nozzle.

3. Experimental design

The experimental system shown in Fig. 2 produced high pressure, underexpanded jet flows at pressures up to 50 MPa with measurements of the gas concentrations along the obstacle plate. In the experiments, helium was used in lieu of hydrogen due to its stable chemical properties and because its physical properties are similar to those of hydrogen. Helium was pumped from storage tanks by a nitrogen powered gas booster into a carbon-fiber tank with a design pressure of 70 MPa. An ER5000 electronic valve then controlled the inlet pressure into the very short nozzle. The 30 cm×30 cm× 0.6 cm obstacle plate was placed vertically in the flow field at the desired distance from the nozzle exit. The plate center was placed at the jet flow centerline with a laser alignment system used to align the plate in the horizontal and vertical directions. A level was used to ensure that the plate was vertical. Six XEN-TCG3880Pt thermal conductivity sensors with accuracies of 2% were mounted on the plate along the vertical direction. The sensors were placed along the vertical centerline 6 cm and 9 cm above and 3 cm, 6 cm and 9 cm below the plate center. The sensors were recessed halfway through the back side of the plate with a 1 mm diameter hole then drilled the rest of the way through the plate. The small diameter was used to reduce the effects of convection in the sensor. All the sensors were connected to an Agilent 34970A data acquisition system with their calibrated voltage signals then converted to helium concentrations. The sensors were calibrated using four standard helium-air concentrations. A 0.5 mm diameter nozzle was used for the experiments. The concentrations were measured for nozzle-plate distances of 0.2 m, 0.3 m and 0.4 m and for a stagnation pressure of 15 MPa.

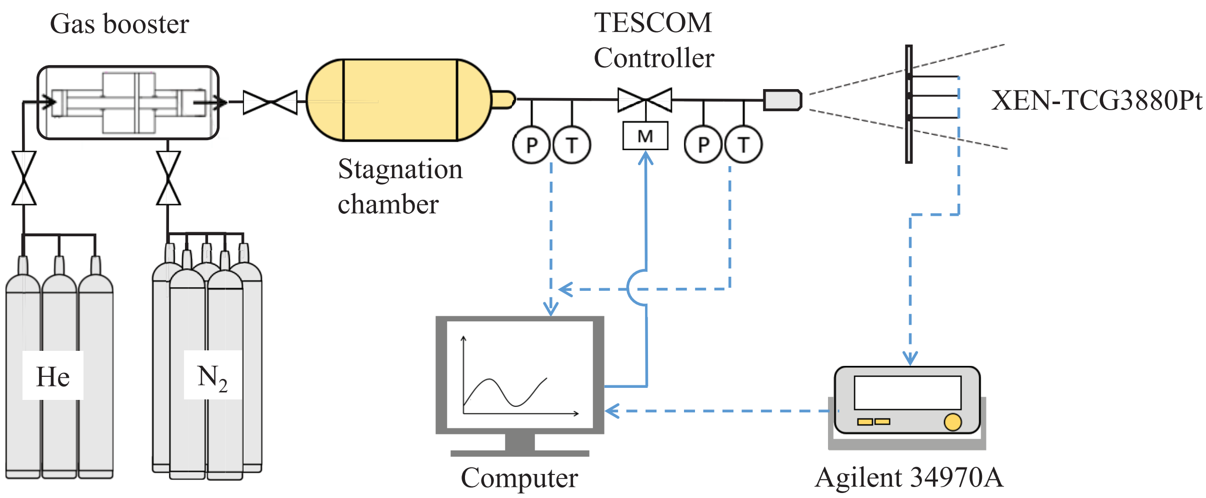

Figure 2: Experimental system layout

4. Numerical Simulations

The flow fields for the high pressure underexpanded jet flows around the plate were modeled with both the full CFD simulation models and the two simplified reduced-order models to predict the helium distributions around the vertical plate. The improved two-layer model was then used to predict the hydrogen profiles around the vertical plate. All the models solved the 3-D Navier-Stokes equations with the k-ω turbulence model and the energy and species equations. Three dimensional numerical simulation geometries was set up for all three simulation models, with the x direction representing the axial direction, y representing the vertical direction and z representing the radial direction. The $z = 0$ plane was used as symmetry to reduce the computational cost with only half of the region ($z > 0$ region) modeled in each case. The simulation started from the inlets of each simulation case and extended 3 cm beyond the outside edges of the plate in all three directions to more accurately predict the gas concentrations along the plate. Fluent 16.0 was used as the numerical solution software. Structured hexagonal meshes were used in all the simulations with the second-order upwind discretization scheme and the k-ω turbulence model. Mesh independence checks were done for each case with the results given for the optimal number of elements in each case. All of the external boundaries in all of the models were set as outlet boundary conditions with zero gauge pressures. The gravity effect was included in all the simulations. The simulations used a compressible air-gas mixture with the density, specific heat, thermal conductivity and viscosity all modeled by ideal gas mixing laws.

4.1. Full CFD Simulations

A diagram of the full CFD simulation geometry and mesh is shown in Figure 3 with an expanded view of the mesh near the inlet.

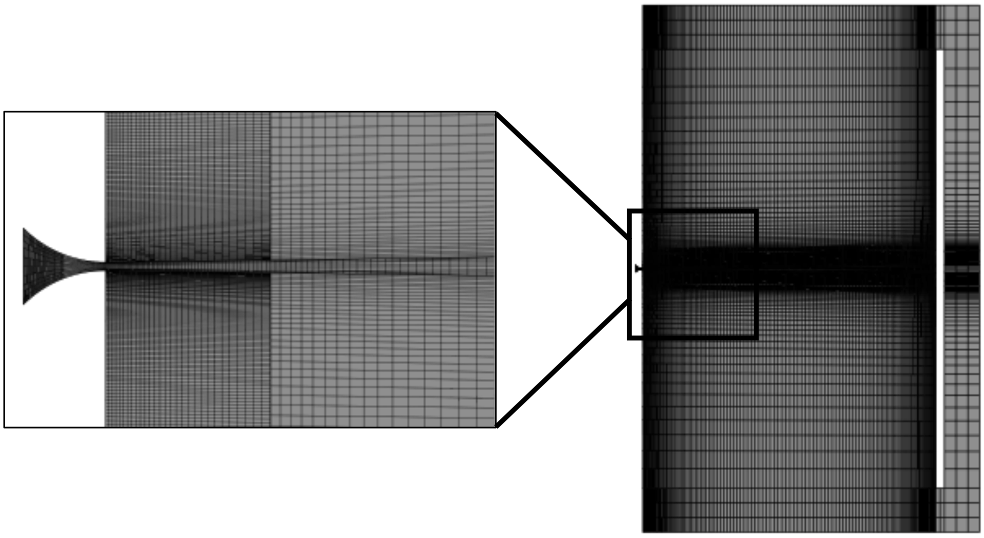

Figure 3: Full CFD model mesh diagram

Since the full CFD simulation model required that the geometry include the whole flow region, the simulation geometry started from the stagnation high pressure inlet. The inlet in the full CFD model simulation geometry was designed as a converging nozzle to improve the flow field at the nozzle exit with the mesh strongly refined in the near nozzle region and near the plate region to improve the accuracy and the convergence. The inlet boundary condition was set to be a pressure inlet with a gauge pressure of 15 MPa and a temperature of 300 K with pure helium or hydrogen. The nozzle exit was set to be located at the $x = 0$ plate with the nozzle center at the origin. The nozzle diameter was set to be 0.5 mm. The density solver was used with the Courant number initially set to 0.1 due to the extremely unstable calculation and slowly increased up to 5 as long as the calculation remained stable. The flow was choked at the nozzle exit and then expanded to a maximum Mach number of about 11 just before the Mach disk. Thus, the flow field included the supersonic jet, the Mach disk and the barrel shocks in the slip region around the supersonic jet. The meshes differed for each nozzle to plate distance but all had 1 to 3 million elements. Mesh independence studies for each plate distance showed that meshes with 1.5 to 2 million elements gave mesh independent results. The y_+ along the plate surface were all less than 5.

4.2. Simplified Model Simulations

The flow field was also modeled numerically using CFD models with the flow input boundary conditions specified by the two simplified models described in Section 2. The simulation geometries for both simplified models did not include the high pressure supersonic region but started with the notional nozzle boundary inlets. Therefore, the whole simulation geometry was cubic and slightly smaller than the full CFD simulation geometry in each case. The mesh details near the inlets for the two simplified models are shown in Figure 4.

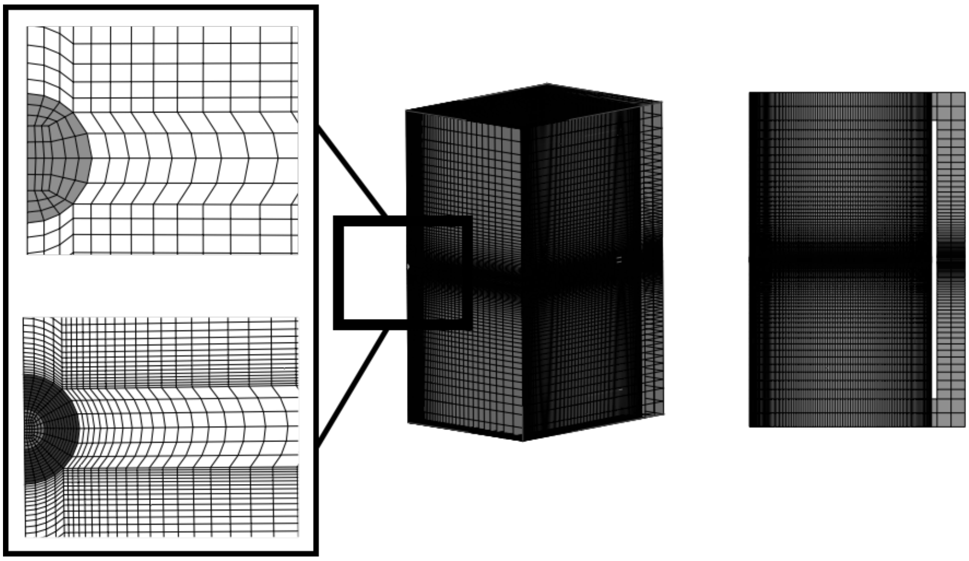

Figure 4: Simplified models mesh diagram: revised Birch87 model (upper-left); improved two-layer model (lower-left); symmetric view (right)

For the improved two-layer model, the boundary inlet condition included two concentric inlets for the Mach disk inlet (light half-circle inlet inside) and the slip region inlet (dark annulus inlet outside the Mach disk inlet). Both inlets had the same axial distance from the real nozzle exit. For the revised Birch87 model, the boundary inlet conditions included one notional nozzle mass inlet. The sole notional nozzle inlet was located at the $x = 0$ plane with the center at the origin, as in the revised Birch87 notional nozzle the axial distance between the real nozzle and notional nozzle neglected as normal. The pressure solver was used for both simplified model cases with the density solver used in some cases as validation. The inlet conditions for the improved two-layer model and the revised Birch87 model cases were both much slower than the velocities in the core region before the Mach disk, so the solutions with the two simplified models were much faster and more stable. The revised Birch87 model simulation geometry had approximately 700,000 elements while the improved two-layer partitioning model simulation geometry had approximately 600,000 elements after the mesh independence studies. The y_+ along the plate surface were all less than 5 for better simulation results.

5. Results and Discussions

5.1. Helium simulations and validation

The nozzle sizes and flow rates for boundary conditions of both the revised Birch87 model and the improved two-layer model are listed in Table 1 for helium flow through a 0.5 mm nozzle from a tank at 15 MPa and 300 K stagnation conditions. The Mach disk in the improved two-layer model is smaller than the notional nozzle in the revised Birch87 model with only 6.8% of the total helium flow rate flowing through the Mach disk (the total helium flow rate through both parts of the improved two-layer model is the same as the helium flow rate through the revised Birch87 notional nozzle). The gas flow rate through the slip region then includes a significant amount of entrained air. The helium molar fraction in the slip region is more than 90%. Given the high molar fraction of helium in the slip region, the notional nozzle obtained using the improved two-layer model can be viewed as a traditional notional nozzle that includes both non-uniform gas velocities and air entrainment. The total diameter of improved two-layer model is less than that given by the revised Birch87 notional nozzle model (2.950 mm for the two-layer model compared with 3.811 mm for the Birch87 model). The axial distance of the notional nozzle from the real nozzle is 4.076 mm for the two-layer model and 0 for the revised Birch87 model.

Table 1: Flow parameters for the two reduced-order models for helium at a stagnation pressure of 15 MPa, stagnation temperature of 300 K and an actual nozzle diameter of 0.5 mm

	Improved two-layer partitioning		Revised Birch87
	Mach disk region	slip region	notional nozzle
diameter/thickness (mm)	1.738	0.606	3.811
gas mass flow (kg/s)	1.81×10^{-4}	4.43×10^{-3}	2.66×10^{-3}
gas temperature (K)	288.5	94.3	300.0
gas mass fraction	1.0	0.56	1.0

The helium simulation results and the experimental data along the vertical plate centerline are compared in Fig. 5 for various obstacle-nozzle distances. The error bars represent the mean standard errors of 3 sets of measurements. With the measurement uncertainty taken into account, the measured helium mass fractions along the centerline are nearly symmetric with the measured helium mass fractions decreasing as both the nozzle-plate distance and the distance from the plate center increase. Throughout the region of interest, the flow is within the momentum dominated region and the measured points show little effect of buoyancy, even for the 40 cm nozzle-plate spacing.

Both the full CFD simulation case and two simplified model cases give reasonable predictions of the helium mass fraction trends along the vertical plate centerline as shown in Fig. 5. All three simulation results show that the helium mass fraction profiles along the center vertical line of the obstacle plate are similar to Gaussian distributions. The increase in the axial distance between the nozzle and the obstacle plate not only reduces the on-plate helium concentrations, but also smooths the distributions. The concentrations drop faster near the vertical centerline than near the lower and upper edges as the nozzle-plate distance increases.

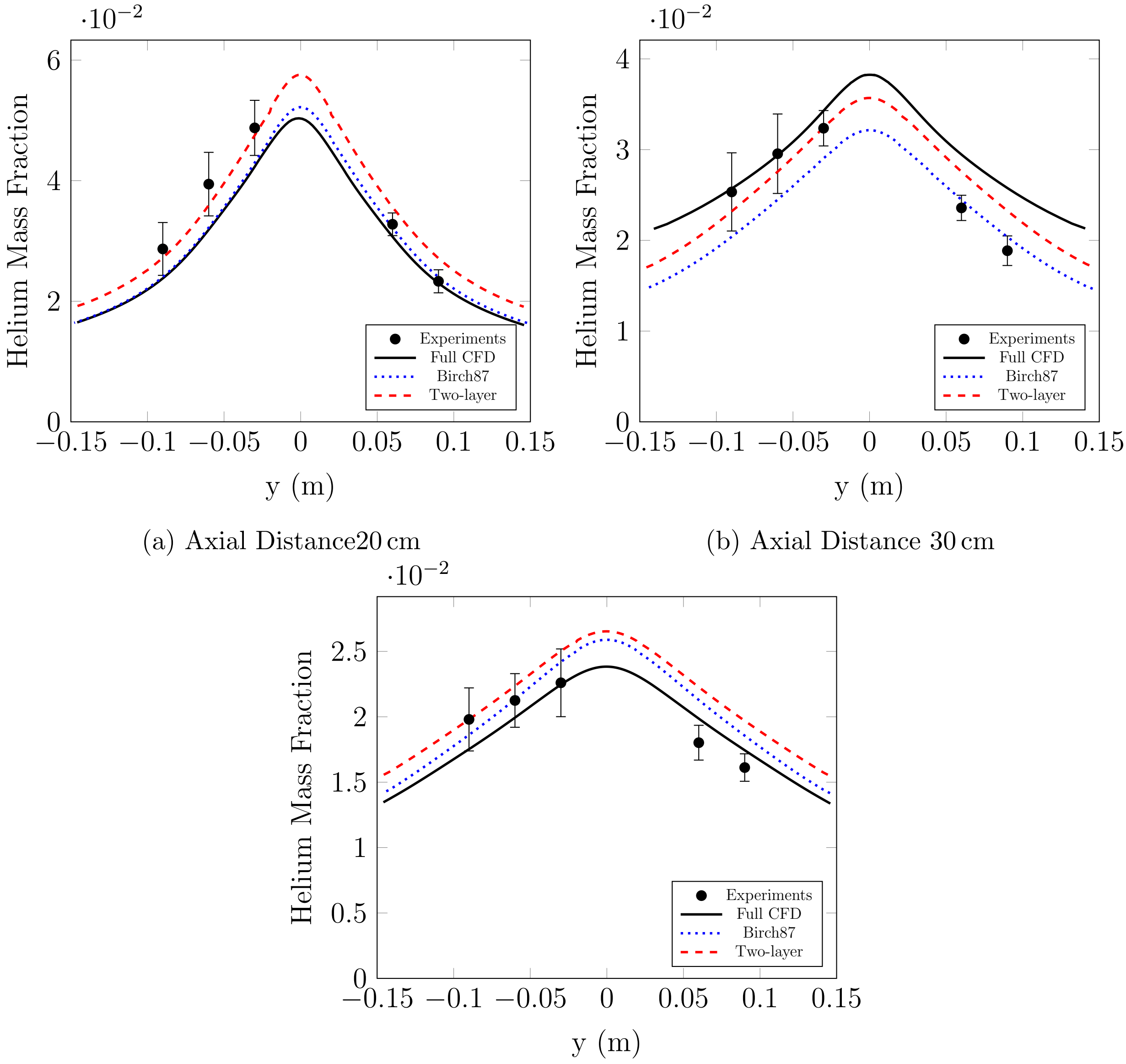

(a) Axial Distance20 cm

(b) Axial Distance 30 cm

(c) Axial Distance 40 cm

Figure 5: Measured and predicted helium mass fractions along the vertical plate centerline

The predictions of the three models are similar. The improved two-layer model case predicts higher concentration profiles than the revised Birch87 model case, with the predictions of the full CFD simulations being both lower and higher than those of the reduced-order models. The improved two-layer model gave better predictions in the lower plate region, while the revised Birch87 model gave better simulation results in the upper plate region. The improved two-layer model gives the best simulation results for the nozzle-plate distance of 20 cm but the simulation accuracy decreases as the axial distance between the real nozzle and the obstacle plate increases. The difference in the accuracies of the three simulation results might also be due to systematic errors in the high pressure experimental system due to errors in positioning the plate and errors in the helium concentration measurements.

For the underexpanded helium jet flow with the obstacle plate, the two-layer simplified model gives good predictions of the on-plate helium concentration profiles. Furthermore, both of the reduced order models required significantly less computing time, on the order of an hour, than the full CFD model (1 $\sim$ 2 weeks) when simulating the geometry with almost the same volume flow region. The simplified models had less elements in the mesh and were able to use the pressure solver which converges much faster. Thus, these results verify the accuracy and efficiency of the improved two-layer model for simulating high pressure helium jet flows with obstacles.

5.2. Hydrogen simulations

The nozzle sizes and flow rates for both the revised Birch87 model and the two-layer model are listed in Table 2 for hydrogen flow through a 0.5 mm nozzle from a tank at 15 MPa and 300 K stagnation conditions. The parameters are similar to those for the helium flows. The flow in the Mach disk region accounts for only 8.7% of the total hydrogen mass flow through the nozzle. The hydrogen mass fraction in the slip region is 52% (94% molar fraction). As in the helium results, the total diameter of the improved two-layer model is smaller than the diameter of the revised Birch87 model (3.45 mm for the two-layer model compared with 3.606 mm for the Birch87 model). The axial distances of both simplified models were the same as for the helium gas models because the Mach disk location is only a function to the pressure ratio as shown in Eq. 15.

Table 2: Flow parameters for the two reduced-order models for hydrogen at a stagnation pressure of 15 MPa, stagnation temperature of 300 K and an actual nozzle diameter of 0.5 mm

	Improved two-layer partitioning		Revised Birch87
	Mach disk region	slip region	notional nozzle
diameter/thickness (mm)	2.130	0.660	3.606
gas mass flow (kg/s)	1.52×10^{-4}	3.08×10^{-3}	1.75×10^{-3}
gas temperature (K)	298.4	136.1	300.0
gas mass fraction	1.0	0.52	1.0

The improved two-layer model predictions for the high pressure hydrogen underexpanded jet flow are shown in Fig. 6 for various nozzle-plate distances. As with the helium simulation results, the predicted hydrogen mass fractions along the vertical centerline of the plate are symmetric around the center. The hydrogen concentration profiles along the plate surface are similar to the simulated helium profiles in Fig. 5 with the hydrogen mass fractions also having shapes similar to Gaussian distributions. When the nozzle-plate axial distance increases the on-plate hydrogen concentration decreases. The region near the center again has larger hydrogen concentration decreases than the changes near the upper and lower parts.

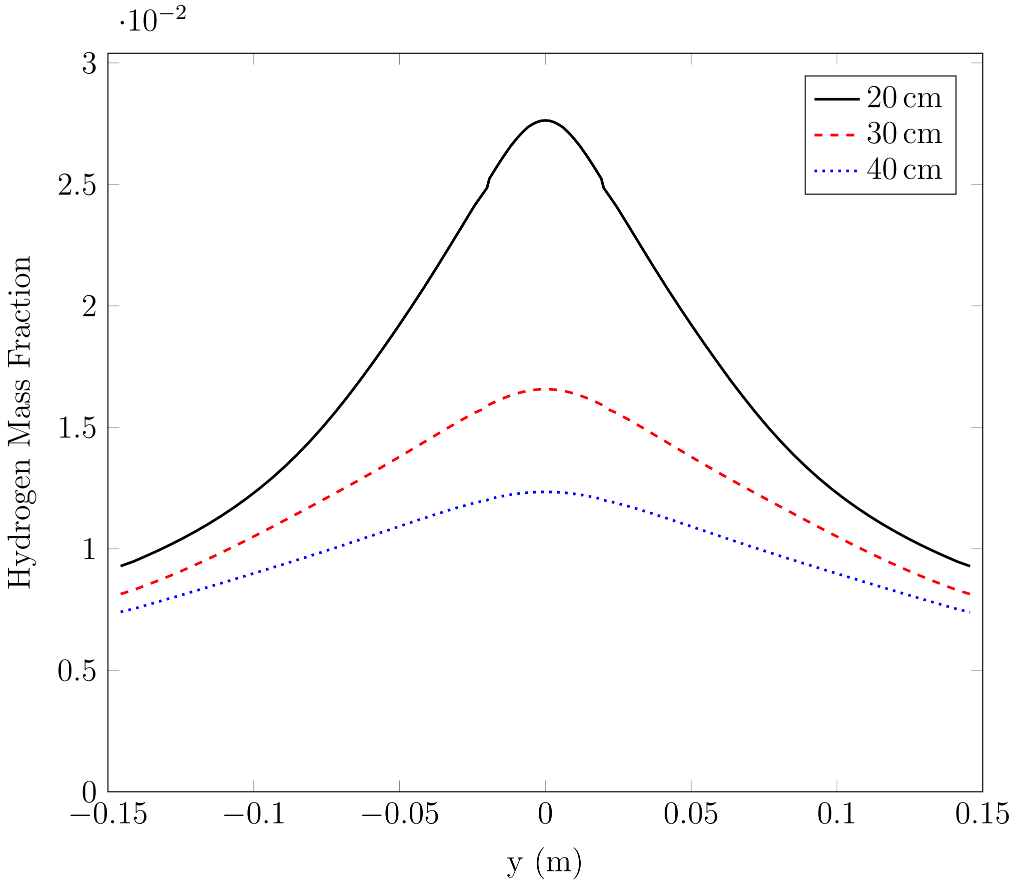

Figure 6: Predicted hydrogen mass fractions along the vertical plate centerline

As shown in Fig. 7, the helium and hydrogen molar concentration profiles along the obstacle vertical centerline predicted by the improved two-layer model are similar. The on-plate improved two-layer predicted hydrogen molar concentrations are slightly lower than the predicted helium concentrations. The differences in the molar concentration increase as the nozzle-plate axial distance increases. This phenomenon is caused by the transition from momentum-dominated flow to buoyancy-dominant flow. When the nozzle-plate distance is small, the jet flow is mainly determined by the initial jet momentum and the gas properties have little effect on the concentration profiles in this region. As the nozzle-plate distance increases, the flow transitions from momentum-dominated to buoyancy-dominated and the gas physical properties have a greater effect on the gas concentration profiles. Given the ability of the two-layer model for simulating the helium concentration profiles, the similarities between the physical properties of helium and hydrogen and the similarities between the predicted profiles, the hydrogen concentrations predicted by the improved two-layer model can be regarded as reliable. Thus, the two-layer model can be used for hydrogen safety assessments due to its accuracy and low computational cost.

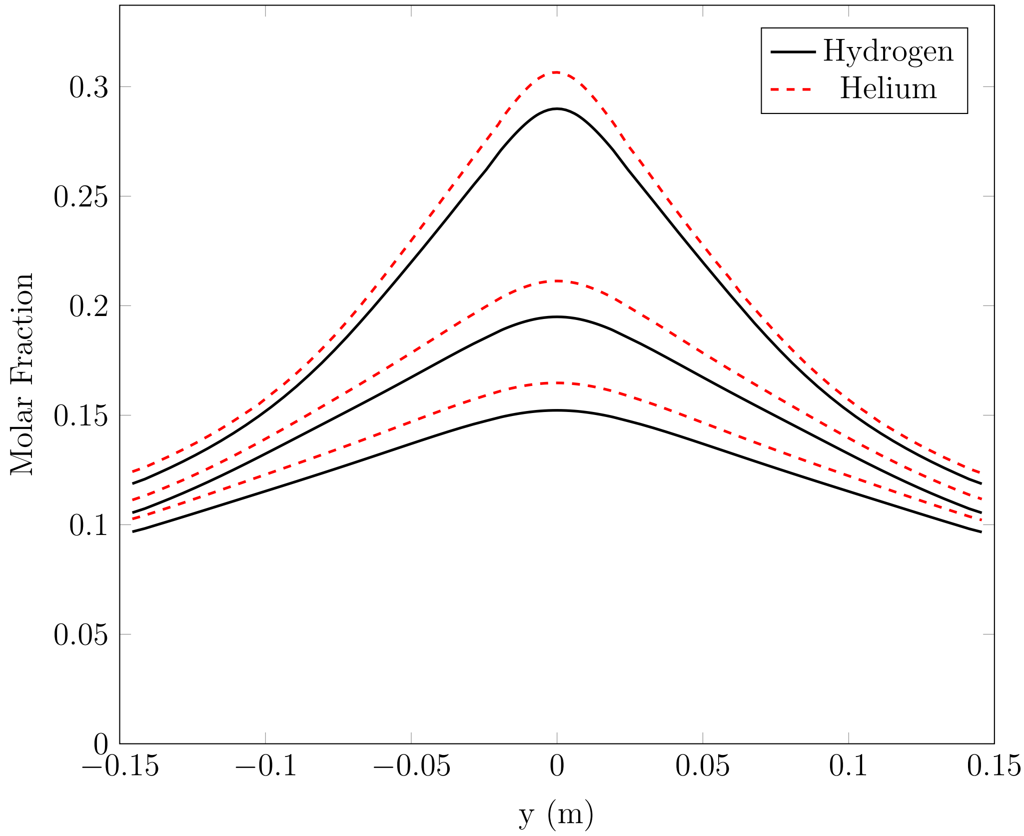

Figure 7: improved two-layer model predicted hydrogen and helium molar concentration along the vertical plate centerline; solid line from top to bottom: hydrogen profiles with axial distance 20, 30 and 40 cm; dashed line from top to bottom: helium profiles with axial distance 20, 30 and 40 cm

6. Conclusions

An improved two-layer partitioning model was developed to simplify the CFD calculation and more efficiently simulate high pressure underexpanded jet flows with a vertical obstacle in the flow field. This improved two-layer model was used to simulate high pressure helium and hydrogen jet flows with a vertical plate in the flow field, along with a full CFD model and an revised version of the Birch87 model which uses the Abel-Noble real gas EOS to take into consideration the real gas properties. The helium simulation results were validated against measured helium mass fraction data for a high pressure jet at 15 MPa. All three models predicted the overall trends of the helium concentration profiles on the plate surface. The predictions of the improved two-layer model had good agreement with the experimental data. The validated improved two-layer model was then used to simulate hydrogen high pressure, underexpanded jet flows with a vertical plate in the flow field. The predicted hydrogen molar concentration profiles were similar to the predicted helium profiles. The two-layer model was also significantly faster than the full CFD simulation (hundreds of times faster) and can serve as a cost-effective method to predict hydrogen leak profiles for hydrogen safety and risk assessment studies.

7. Acknowledgements

This research was supported by the National Natural Science Foundation of China, Grant No. 51476091 and 51706125 and by the Science Fund for Creative Research Groups of the National Natural Science Foundation of China, Grant No. 51321002. The work was also sponsored by the Shandong Provincial Natural Science Foundation, China, Grant No. ZR2017BEE003 and the China Postdoctoral Science Foundation, Grant No. 2017M612267.

References

[1] P. Cumber, M. Fairweather, S. Falle, J. Giddings, Predictions of the structure of turbulent, highly underexpanded jets, Journal of Fluids engineering 117 (4) (1995) 599–604.

[2] C. d. Donaldson, R. S. Snedeker, A study of free jet impingement. part 1. mean properties of free and impinging jets, Journal of Fluid Mechanics 45 (2) (1971) 281319. doi:10.1017/S0022112071000053.

[3] J. Wilkes Inman, P. Danehy, R. Nowak, D. Alderfer, Fluorescence imaging study of impinging underexpanded jets, in: 46th AIAA Aerospace Sciences Meeting and Exhibit, p. 619.

[4] J. Palmer, R. Hansont, Application of method of characteristics to underexpanded, freejet flows with vibrational nonequilibrium, AIAA journal 36 (2) (1998) 193–200.

[5] A. J. Saddington, N. J. Lawson, K. Knowles, An experimental and numerical investigation of under-expanded turbulent jets, The Aeronautical Journal (1968) 108 (1081) (2004) 145152. doi:10.1017/S0001924000151590.

[6] T. A. Jr., On the structure of jets from highly underexpanded nozzles into still air, Journal of the Aerospace sciences 26 (1) (1959) 16–24.

[7] T. Matsuda, y. Umeda, R. Ishii, k. Sawada, Numerical and experimental studies on choked underexpanded jets, in: 19th AIAA, Fluid Dynamics, Plasma Dynamics, and Lasers Conference, 1987, p. 1378.

[8] T. Rogers, P. Petersen, L. Koopmans, P. Lappas, A. Boretti, Structural characteristics of hydrogen and compressed natural gas fuel jets, International Journal of Hydrogen Energy 40 (3) (2015) 1584 – 1597. doi:https://doi.org/10.1016/j.ijhydene.2014.10.140.
URL `http://www.sciencedirect.com/science/article/pii/S036031991403016X`

[9] N. J. Dam, M. Rodenburg, R. A. L. Tolboom, G. G. M. Stoffels, P. M. Huisman-Kleinherenbrink, J. J. ter Meulen, Imaging of an underexpanded nozzle flow by uv laser rayleigh scattering, Experiments in Fluids 24 (2) (1998) 93–101. doi:10.1007/s003480050156.
URL `https://doi.org/10.1007/s003480050156`

[10] B. Ewan, K. Moodie, Structure and velocity measurements in underexpanded jets, Combustion Science and Technology 45 (5-6) (1986) 275–288.

[11] E. Franquet, V. Perrier, S. Gibout, P. Bruel, Free underexpanded jets in a quiescent medium: A review, Progress in Aerospace Sciences 77 (2015) 25–53. doi:https://doi.org/10.1016/j.paerosci.2015.06.006.

[12] B. Xu, L. El Hima, J. X. Wen, S. Dembele, V. Tam, T. Donchev, Numerical study on the spontaneous ignition of pressurized hydrogen release through a tube into air, Journal of Loss Prevention in the Process Industries 21 (2) (2008) 205–213.

[13] M. Thring, M. Newby, Combustion length of enclosed turbulent jet flames, Symposium (International) on Combustion 4 (1) (1953) 789 – 796, fourth Symposium (International) on Combustion. doi:https://doi.org/10.1016/S0082-0784(53)80103-7.

[14] A. Birch, D. Brown, M. Dodson, F. Swaffield, The structure and concentration decay of high pressure jets of natural gas, Combustion Science and technology 36 (5-6) (1984) 249–261.

[15] J. P. Gore, G. M. Faeth, D. Evans, D. B. Pfenning, Structure and radiation properties of large-scale natural gas/air diffusion flames, Fire and Materials 10 (3-4) (1986) 161–169. doi:10.1002/fam.810100311.

[16] A. Birch, D. Hughes, F. Swaffield, Velocity decay of high pressure jets, Combustion Science and Technology 52 (1-3) (1987) 161–171.

[17] X. Li, D. M. Christopher, E. S. Hecht, I. W. Ekoto, Comparison of two-layer model for hydrogen and helium jets with notional nozzle model predictions and experimental data for pressures up to 35 mpa, International Journal of Hydrogen Energy 42 (11) (2017) 7457–7466.

[18] E. Hecht, X. Li, I. W. Ekoto, Validated equivalent source model for an underexpanded hydrogen jet, Report, Sandia National Laboratories (SNL-CA), Livermore, CA (United States) (2015).

[19] K. B. Yüceil, M. V. Ötügen, Scaling parameters for underexpanded supersonic jets, Physics of Fluids 14 (12) (2002) 4206–4215.

[20] K. Harstad, J. Bellan, Global analysis and parametric dependencies for potential unintended hydrogen-fuel releases, Combustion and Flame 144 (12) (2006) 89–102. doi:https://doi.org/10.1016/j.combustflame.2005.07.005.

[21] V. Molkov, Fundamentals of hydrogen safety engineering ii-ebooks and textbooks from bookboon.com (2012).

[22] V. Molkov, Hydrogen safety engineering: the state-of-the-art and future progress.

[23] A. J. Ruggles, I. W. Ekoto, Ignitability and mixing of underexpanded hydrogen jets, International Journal of Hydrogen Energy 37 (22) (2012) 17549–17560. doi:https://doi.org/10.1016/j.ijhydene.2012.03.063.

[24] S. H. Han, D. Chang, J. S. Kim, Release characteristics of highly pressurized hydrogen through a small hole, International Journal of Hydrogen Energy 38 (8) (2013) 3503–3512.

[25] X. Li, D. M. Christopher, Dispersion of high pressure underexpanded helium jets into the atmosphere, in: 15^{th} International Heat Transfer Conference, paper 159337, Japan.

[26] I. A. Johnston, The NOBLE-ABEL equation of state: Thermodynamic derivations for ballistics modelling, Tech. rep., Defence Science and Technology Organisation Edinburgh (Australia) Weapons Systems Div (2005).

[27] A. Velikorodny, S. Kudriakov, Numerical study of the near-field of highly underexpanded turbulent gas jets, International Journal of Hydrogen Energy 37 (22) (2012) 17390–17399.

[28] X. Li, Study of subsonic and high pressure, underexpanded hydrogen jets, Thesis (2015).

[29] C. Zhao, Y. Jiang, Gas jet flow dynamics (1998).